

ARTICLE

Received 17 Jun 2013 | Accepted 8 Nov 2013 | Published 27 Nov 2013

DOI: 10.1038/ncomms3899

Pits confined in ultrathin cerium(IV) oxide for studying catalytic centers in carbon monoxide oxidation

Yongfu Sun^{1,*}, Qinghua Liu^{2,*}, Shan Gao¹, Hao Cheng², Fengcai Lei¹, Zhihu Sun², Yong Jiang², Haibin Su³, Shiqiang Wei² & Yi Xie¹

Finding ideal material models for studying the role of catalytic active sites remains a great challenge. Here we propose pits confined in an atomically thin sheet as a platform to evaluate carbon monoxide catalytic oxidation at various sites. The artificial three-atomic-layer thin cerium(IV) oxide sheet with approximately 20% pits occupancy possesses abundant pit-surrounding cerium sites having average coordination numbers of 4.6 as revealed by X-ray absorption spectroscopy. Density-functional calculations disclose that the four- and five-fold coordinated pit-surrounding cerium sites assume their respective role in carbon monoxide adsorption and oxygen activation, which lowers the activation barrier and avoids catalytic poisoning. Moreover, the presence of coordination-unsaturated cerium sites increases the carrier density and facilitates carbon monoxide diffusion along the two-dimensional conducting channels of surface pits. The atomically thin sheet with surface-confined pits exhibits lower apparent activation energy than the bulk material (61.7 versus 122.9 kJ mol⁻¹), leading to reduced conversion temperature and enhanced carbon monoxide catalytic ability.

¹Hefei National Laboratory for Physical Sciences at Microscale, Collaborative Innovation Centre of Chemistry for Energy Materials, University of Science and Technology of China, Hefei 230026, China. ²National Synchrotron Radiation Laboratory, University of Science and Technology of China, Hefei, Anhui 230029, China. ³Division of Materials Science, Nanyang Technological University, 50 Nanyang Avenue, Singapore 639798, Singapore. * These authors contributed equally to this work. Correspondence and requests for materials should be addressed to Y.X. (email: yxie@ustc.edu.cn) or to S.W. (email: sqwei@ustc.edu.cn).

Catalysis can accelerate the speed of chemical reactions through changing the reaction pathway and lowering the activation energy, hence its wide application in diverse fields such as industrial ammonia production in Haber process¹, the catalytic converters in automobiles² and the enzymatic catalytic processes in living systems³. According to the basic theory originally proposed by Taylor, in gas-phase catalytic systems⁴, catalytic reactions usually occur at the active sites of catalysts, for which the crystalline defects such as step edges and kink sites with low coordination numbers are the favourable catalytic reaction centres^{5–8}. Heterogeneous processes, generally consist of three consecutive steps of adsorption, chemical reaction and desorption, and the corresponding catalytic rate is often limited by one elementary step, referred to the rate-determining step^{8,9}. Taking the extensively studied catalytic CO oxidation as an example, the catalytic reaction rate is typically limited by the adsorption and dissociation of O₂ molecules on the active sites of catalysts¹⁰.

Up to now, various reaction mechanisms for CO oxidation have been proposed, among which the three most popular mechanisms are the Langmuir-Hinshelwood mechanism^{8,11,12}, the Eley-Rideal mechanism^{8,13} and the Mars-van Krevelen mechanism¹⁴. Although these mechanisms have been proposed to investigate the catalytic reaction processes, atomic-level insights into the underlying mechanism of catalysis are less explored. This is mainly due to the large differences between idealized models and real catalysts, and hence the knowledge gained from these models is not readily applicable to real catalysts. To evaluate where catalysis occurs and which site has the highest activity, simplifying and bridging the catalyst model with the real catalyst is of paramount importance. Recently, for better understanding the fundamental mechanism in catalytic CO oxidation, reactions on oriented crystals with a predominantly exposed facet have been further explored^{15–23}, thanks to the single active site on these facets. For instance, theoretical calculations revealed that CO had stronger chemisorption on the {110} and {100} facets of CeO₂ than on the {111} facets^{17,18}. This has been experimentally demonstrated by the fact that the rod-like CeO₂ exposing {110} and {100} facets showed obviously improved CO catalytic properties than octahedron-like CeO₂ exposing {111} facets¹⁹. Also, Xie *et al.*²⁰ observed that the cube-like CeO₂ crystals with exposed {100} facets exhibited superior CO oxidation properties than the truncated octahedron-like CeO₂ crystals with exposed {100} and {111} facets. Although the unique crystal plane has provided a good platform for understanding the role of active sites in catalysis, the relatively low ratio of surface active sites to the total atom numbers makes the quantification of a model-performance relationship a great challenge (Fig. 1a). Fortunately, recent studies have revealed that nanoscale crystallites such as CeO₂ nanostructures are beneficial to the CO oxidation reaction thanks to their downsizing effect^{24–29}. For example, Botana *et al.*²⁵ have found that CeO₂ nanotubes exhibited 400-fold higher CO oxidation compared to polycrystalline CeO₂ powder owing to their superior redox properties. Also, Tsang *et al.* have demonstrated that the quantum size effect could enable the nanosize CeO₂ (below 5 nm) to possess dramatically increased surface superoxide species³⁰, which undoubtedly contributed to improve the catalytic oxidation activity^{30–32}. In addition, Cormatt *et al.* have illustrated that nanocrystalline CeO₂ could increase the activity of Au for CO oxidation by two orders of magnitude through effectively adsorbing and activating O₂ molecules²⁴. These results indicated that nanoscale size effects could provide more active sites and hence helped to improve the catalytic properties^{33,34}. Hence, developing a material model with exposed unique crystal plane as well as nanoscale thickness holds the key to disclosing the role of active sites in catalysis.

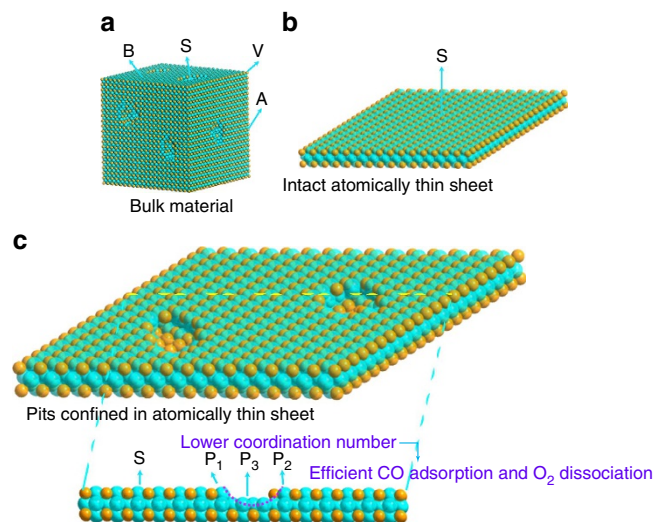


Figure 1 | Schematic illustration for evaluating catalysis location and activity. (a) Bulk CeO₂; (b) intact and (c) atomically thin CeO₂ sheets with surface-confined pits; P₁ and P₂ stand for the representative pit-surrounding surface Ce sites, while P₃ represents the bottom Ce site of the pit; S stands for the surface Ce site of atomically thin sheet and around the defects of bulk material; A, V and B represent the aris, vertex and surface Ce sites of bulk material, respectively.

In this work, taking the typical CO oxidation catalyst of CeO₂ as an example, an ideal model consisting of intact atomically thin CeO₂ sheets is developed to maximize the number of coordinately unsaturated active sites, as shown in Fig. 1b. Due to the atomic thickness and specific surface area, such sheets possess the features of relatively disperse active sites and a high ratio of surface active sites to the total atom numbers. To further promote the activity of the catalytic sites, we can make lots of artificial pits with lower coordination numbers on the surface of atomically thin CeO₂ sheets (Fig. 1c). To date, it remains particularly challenging to synthesize atomically thin CeO₂ sheets with surface-confined pits in a controllable manner, due to the difficulty in bond-cleavage and the absence of an intrinsic driving force for the formation of coordinately unsaturated active sites^{7,8}. To meet this challenge, we herein develop an ‘ultrafast open space transformation’ strategy and successfully synthesize three-atom-layer thin CeO₂ sheets with ~20% pits occupancy. X-ray absorption fine structure spectroscopy (XAFS) and density-functional calculations (DFT) disclose that the pit-surrounding Ce sites with average Ce-O coordination numbers as low as 4.6 serve as the catalytically active centres. These centres play essential roles in O₂ activation, CO adsorption and diffusion, which lead to decreased apparent activation energy from 122.9 to 61.7 kJ mol⁻¹ as well as obviously reduced CO conversion temperatures. This study provides valuable insights into the role of active centres in catalysis through a semi-quantitative model-structure-performance relationship, holding great promise for designing catalysts with highly efficient active centres.

Results

Characterization of ultrathin CeO₂ sheets with surface pits. As depicted in Fig. 2a and Supplementary Fig. S1, the successful synthesis of ultrathin CeO₂ sheets took advantage of an intermediate precursor of ultrathin CeCO₃OH sheets. During the formation of this precursor, the peculiar arrangement of oleate ions around the surface of Ce³⁺ played a vital role: Ce³⁺ initially interacted with oleate ions to form Ce-oleate complexes *via* an

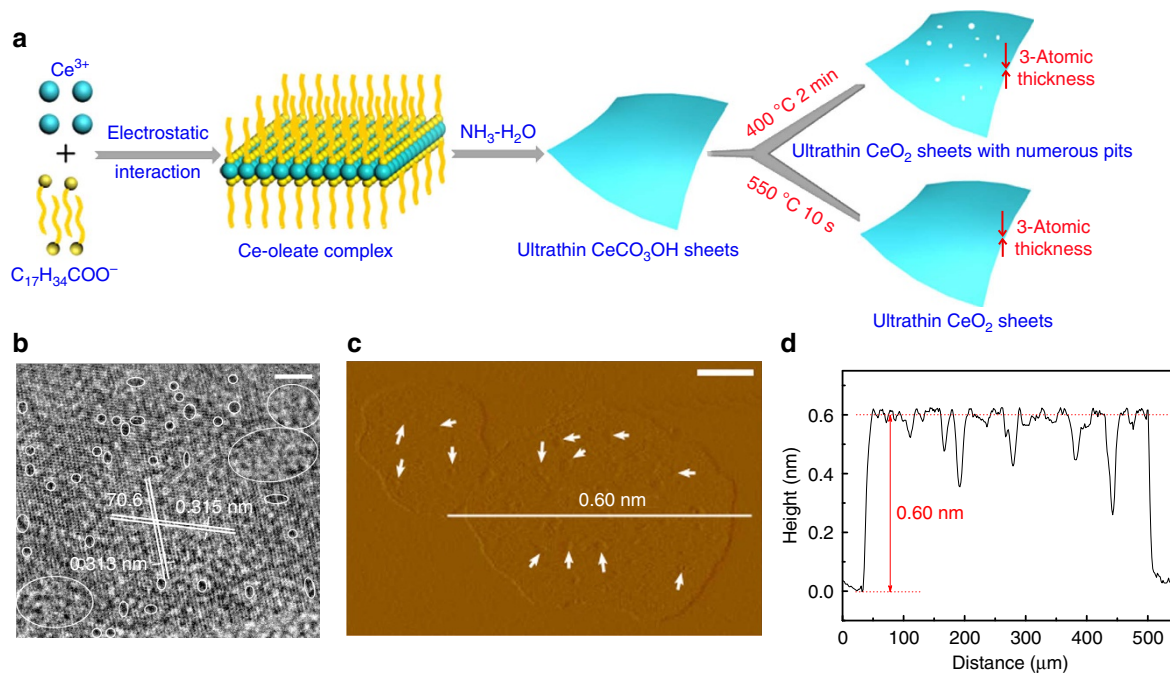


Figure 2 | Formation process and characterization of the ultrathin CeO₂ sheets with numerous surface pits. (a) Schematic illustration for the formation of ultrathin CeO₂ sheets with numerous surface pits and intact ultrathin CeO₂ sheets. Note that the heating temperature and time have a vital role in the formation of pits on their surface. (b–d) Characterizations for the three-atom-thin CeO₂ sheets with numerous surface pits: (b) HRTEM image, (c) AFM image and (d) the height profile along the white line indicated in (c). The scale bars in (c) and (d) are 3 and 100 nm, respectively. The inset circles and arrows in (b) and (c) denote the presence of pits on their surface.

electrostatic interaction and hence assembled into atomically thin two-dimensional structure driven by the hydrophobic effect of oleate tails³⁵. After addition of NH₃·H₂O followed by hydrothermal treatment for 48 h, the ultrathin CeCO₃OH sheets were obtained and fully characterized in Supplementary Fig. S2. And then, direct heating of the precursor at 400 °C for 2 min in air not only resulted in the formation of clean three-atom-layer thin CeO₂ sheets, but also brought on numerous pits on their surfaces (Fig. 2b–d and Supplementary Figs S3–S5). The high-resolution transmission electron microscopy (TEM) image in Fig. 2b clearly revealed the high [110] orientation of the CeO₂ sheets, while the atomic force microscopy (AFM) image and the corresponding height profile in Fig. 2c,d showed their height of about 0.60 nm, which fairly agreed with the 0.57 nm thickness of three-atom-thin CeO₂ slab along the [110] direction. More importantly, the HRTEM and AFM images in Fig. 2b–d also depicted that the pits possessed an occupancy of about 20% in the three-atom-thick CeO₂ sheets, indicating the presence of abundant pit-surrounding Ce sites. By contrast, the heating at higher temperature of 550 °C with a shorter time of 10 s only resulted in the formation of clean three-atom-thick CeO₂ sheets without surface pits (Fig. 2a and Supplementary Fig. S6), strongly suggesting that the heating temperature and time played an important role in the formation of pits on the surfaces of ultrathin CeO₂ sheets (Supplementary Figs S7–S9).

Synchrotron radiation XAFS measurements. To obtain quantitative structural parameters around the pits of the three-atom-thick CeO₂ sheets, XAFS measurements at Ce L₃-edge were carried out at the U7C beamline of the National Synchrotron Radiation Laboratory, China. As shown in Fig. 3a, the Ce L₃-edge $k^2\chi(k)$ oscillation curve for the ultrathin CeO₂ sheets with numerous surface pits displayed obvious differences

compared with the ultrathin CeO₂ sheets and bulk CeO₂ (Supplementary Fig. S10). This was further verified by their corresponding Fourier transformed (FT) $k^2\chi(k)$ functions in Fig. 3b, which displayed that the two main peaks gradually shifted to the low R direction along with obviously decreased intensities, qualitatively revealing their distinct local atomic arrangement. Moreover, to achieve quantitative structural parameters around Ce atoms, a least-squares curve fitting was conducted and the details of the EXAFS data fitting are provided in the Methods section. As for the ultrathin CeO₂ sheets, Table 1 revealed that the distances and coordination numbers for Ce–O, Ce–Ce, Ce–O–O and Ce–Ce–O coordinations reduced remarkably, while their disorder degrees increased significantly as compared with bulk counterpart, suggesting a noticeable distortion on their surface. Importantly, the pit-surrounding Ce–O distances, confined in the ultrathin CeO₂ sheets with numerous surface pits, were contracted from 2.327 to 2.302 Å, and their coordination numbers remarkably decreased from 6.5 to 4.6, associated with significantly increased disorder degrees relative to the ultrathin CeO₂ sheets (Table 1). This implied an obvious distortion surrounding the pits of ultrathin CeO₂ sheets. Notably, such surface distortion has already been observed in previously reported atomically thin two-dimensional sheets and has also been demonstrated to endow them with excellent structural stability and increased states density^{6,7,36}. As depicted by the calculated densities of states in Fig. 3c, the presence of abundant coordination-unsaturated pit-surrounding Ce sites in the ultrathin CeO₂ sheets led to the formation of defect states near the Fermi level, which resulted in an obvious increase of hole carrier concentration with respect to the ultrathin CeO₂ sheets and bulk counterpart³⁷. As will be shown, these features enabled the ultrathin CeO₂ sheets with numerous surface pits to realize fast CO diffusion along the two-dimensional conducting channel of surface pits and hence improved their CO catalytic properties^{6,7,38}.

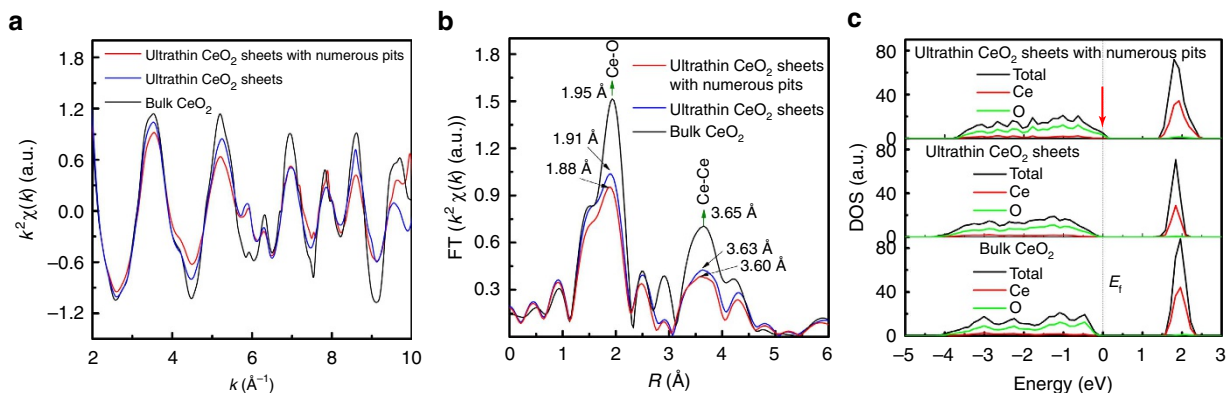


Figure 3 | Synchrotron radiation XAFS measurements. (a) Ce L_3 -edge extended XAFS oscillation function $k^2\chi(k)$, (b) the corresponding Fourier transforms $FT(k^2\chi(k))$, (c) the calculated densities of states for the ultrathin CeO₂ sheets with numerous surface pits, ultrathin CeO₂ sheets and bulk CeO₂, respectively. a.u., arbitrary unit.

Table 1 | EXAFS curve-fitting results.

Sample	Path	R (Å)	N	σ^2 (10^{-3}Å^2)	ΔE_0 (eV)
Bulk CeO ₂	Ce-O	2.344	8.0	4.7	2.9
	Ce-Ce	3.827	12.0	6.3	4.2
	Ce-O-O	3.697	24.0	5.9	3.3
	Ce-Ce-O	4.257	48.0	6.8	3.7
Ultrathin CeO ₂ sheets	Ce-O	2.327	6.5 (6.7)	5.0	2.9
	Ce-Ce	3.812	7.7 (8.0)	6.7	4.5
	Ce-O-O	3.667	16.8 (17.3)	7.4	3.2
	Ce-Ce-O	4.234	29.7 (32.0)	9.0	3.4
Ultrathin CeO ₂ sheets with numerous pits	Ce-O(80% remain)	2.327	6.5 (6.7)	5.6	2.7
	Ce-O(20% shrink)	2.302	4.6 (4.7)	8.3	3.0
	Ce-Ce	3.802	7.4 (7.8)	8.3	4.6
	Ce-O-O	3.644	15.1 (15.5)	8.7	3.3
	Ce-Ce-O	4.212	28.5 (30.3)	9.2	3.4

Structural parameters around Ce atoms extracted from EXAFS curve-fitting for the ultrathin CeO₂ sheets with numerous surface pits, ultrathin CeO₂ sheets and bulk CeO₂, respectively. The coordination numbers in brackets correspond to the ideal average coordination numbers of exterior and interior atoms for the ultrathin CeO₂ sheets with three-atomic-layer thicknesses.

Catalytic carbon monoxide oxidation. Summarizing the above XAFS, TEM and AFM results, an ideal model for three-atom-thick CeO₂ sheets with surface-confined pits is built to gain atomic-level insights into the underlying catalytic mechanism (Fig. 4c). According to the widely accepted Langmuir-Hinshelwood mechanism^{8,11,12}, the CO oxidation occurring on the pit-surrounding Ce sites may consist of the following elementary steps: (1) Adsorption of CO and O₂ molecules from the gas phase onto the pit-surrounding Ce sites; (2) dissociation of O₂ molecules on the pit-surrounding Ce sites; (3) reaction between CO and dissociated O atom to form CO₂; (4) desorption of CO₂ to the gas phase. In addition, it is noticeable that CO should diffuse to the nearby atomic O before their reaction to form CO₂, in which the CO molecules need to overcome a diffusion barrier^{39,40}. DFT calculations were performed on various pit-surrounding Ce sites and on-surface Ce sites in order to identify the active sites. Figure 4a clearly revealed that CO and O₂ molecules exhibited the highest adsorptive energies (absolute values) at pit-surrounding 4-coordinated Ce site (P₂, -1.25 eV) and 5-coordinated Ce site (P₁, -1.75 eV), respectively. This indicated that the CO and O₂ molecules preferred to adsorb at the pit-surrounding Ce sites with different coordination numbers and hence would not block the active sites for each other, thus effectively avoiding the catalyst poisoning. Also, the dissociation of O₂ molecules needed the lowest activation energy of 0.46 eV at the two adjacent 5-coordinated Ce sites (2P₁, Fig. 4b), suggesting

that they preferably dissociated into oxygen atoms on the dual adjacent fivefold coordinated Ce sites and their corresponding transition state was shown in Fig. 4c. Considering the relatively small energy barrier of 0.12 eV for the CO+O associative desorption, it was suggested that the bonding strength for O atoms at the pit-surrounding Ce sites was optimum and would make these sites active⁵. The above results revealed that the coordination number and spatial distribution of the pit-surrounding Ce sites played a crucial role in CO catalytic oxidation. In this case, the pits with different size and shape would theoretically achieve the similar CO adsorption energies and O₂ activation energies when their pits could provide the 4- and 5-coordinated pit-surrounding Ce sites with similar percentage and spatial distribution (Supplementary Fig. S11). Moreover, the CO diffusion barriers on the pit-surrounding Ce sites and on-surface Ce sites were calculated to be 0.08 and 0.17 eV, respectively. The lowered CO diffusion barrier on the pit-surrounding Ce sites could be benefited from their increased states density near the Fermi level (Fig. 3c) and hence contributed to lower the overall activation energy, thus finally improving their CO oxidation activity. In this case, the adsorbed CO molecules at 4-coordinated Ce site could effectively diffuse into the 5-coordinated Ce site along the two-dimensional conducting channel of surface pits and hence reacted with the dissociated oxygen atoms to produce CO₂. Thus, although it was difficult to distinguish the rate-determining step and accurately evaluate the

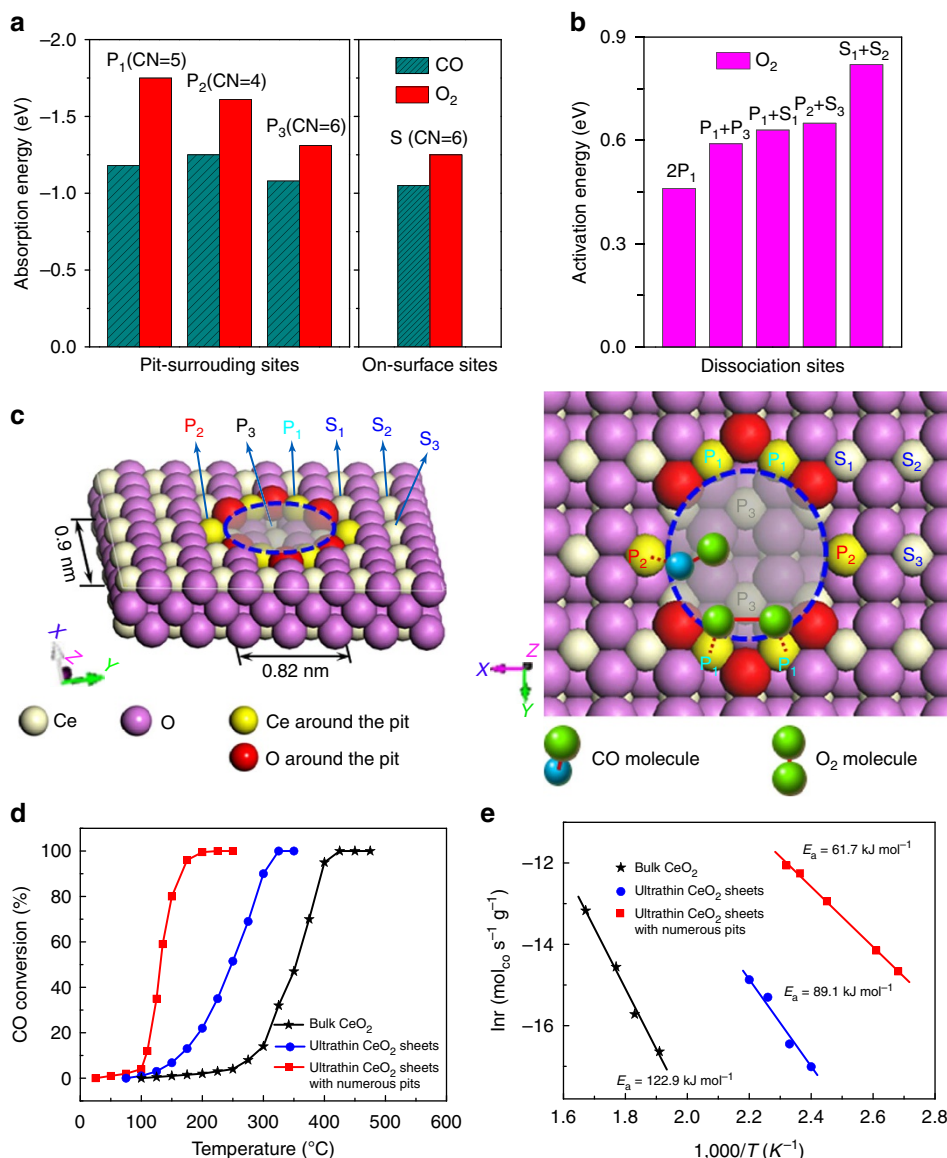


Figure 4 | Catalytic carbon monoxide oxidation. (a) Calculated adsorption energies for CO and O₂ molecules on the pit-surrounding Ce sites (P₁~P₃) and on-surface Ce sites (S₁~S₃), and (b) calculated activation energies for O₂ dissociation on the adjacent Ce sites of ultrathin CeO₂ sheets with numerous pits; the coordination numbers of P₁, P₂, P₃, S₁, S₂ and S₃ are 5, 4, 6, 6 and 6, respectively. (c) Overhead and top views of schematic structures for the three-atom-thick CeO₂ sheets with a pit size of 0.90 nm × 0.82 nm (This size is fairly consistent with that statistically calculated from the HRTEM image in Fig. 2b); the CO molecules prefer to adsorb at P₂ site, while the O₂ molecules tend to adsorb and dissociate at the adjacent P₁ sites. (d) Catalytic activity for CO oxidation versus reaction temperatures (experimental error: ±3%) and (e) the corresponding Arrhenius plot for the three CeO₂ samples (experimental error: ±3%).

overall activation energy without full kinetic simulations, the simple analysis of the above activation energies helped to draw the following conclusions: (1) The step of O₂ activation was the rate-limiting step for the ultrathin CeO₂ sheets with numerous surface pits, since the calculated O₂ activation energy of ~0.46 eV on the pit-surrounding Ce sites was much higher than the corresponding calculated CO + O associative desorption energy (0.12 eV) and the CO diffusion energy (0.08 eV); (2) the overall activation energy on the pit-surrounding Ce sites could be roughly evaluated to be the value between 0.46 and 0.66 eV (corresponding to the range from 44.4 to 63.6 kJ mol⁻¹), fairly consistent with their apparent activation energy of 61.7 kJ mol⁻¹ in Fig. 4e. Based on the above results, one could conclude that the ultrathin CeO₂ sheets with numerous surface pits had ~20% pits occupancy, in which the abundant pit-surrounding Ce sites

served as the active sites in CO catalytic oxidation and such a large amount of highly active pit-surrounding Ce sites could in fact support them to quickly complete the CO catalytic oxidation at a low reaction temperature (Fig. 4d). By contrast, for the intact ultrathin CeO₂ sheets without surface pits and bulk counterpart (Supplementary Figs S6 and S10), only the surface Ce atoms could serve as the active sites to catalyse CO oxidation. Note that the pit-surrounding Ce site has an average coordination number of 4.6, much smaller than that (6.5) of the surface Ce site in the ultrathin CeO₂ sheets (Fig. 3), reasonably exhibiting higher catalytic activity than that at the on-surface Ce site. The conclusion could be further confirmed by their corresponding adsorption energies for CO and O₂ molecules as well as O₂ dissociation energies in Fig 4a,b. In this case, the ultrathin CeO₂ sheets with numerous surface pits could theoretically possess

lowered overall activation energy as well as accelerated catalytic reaction rate compared with the ultrathin CeO₂ sheets without surface pits and the bulk counterpart.

To verify the predictions from the above theoretical model, the corresponding CO catalytic properties of the ultrathin CeO₂ sheets with numerous surface pits were investigated. As shown in Fig. 4d, they possessed 50% CO conversion at 131 °C, which was 117 °C and 223 °C lower than that of the ultrathin CeO₂ sheets and bulk counterpart, respectively. At the same temperature of 131 °C, the ultrathin CeO₂ sheets and bulk CeO₂ only showed CO conversion ratio of 3.2 and 0.89%, over 15 and 50 times smaller than that of the ultrathin CeO₂ sheets with numerous surface pits. Also, the complete CO conversion temperature for the ultrathin CeO₂ sheets with numerous surface pits was about 200 °C, strikingly lower than that of the ultrathin CeO₂ sheets (325 °C) and bulk counterpart (425 °C). To the best of our knowledge, the half conversion temperature for the ultrathin CeO₂ sheets with numerous surface pits was much lower than all of those reported values for parent CeO₂ (refs 41–44), strongly suggesting the remarkably improved low-temperature CO catalytic activity. Moreover, the Arrhenius plot in Fig. 4e revealed that the apparent activation energy for the ultrathin CeO₂ sheets with numerous surface pits was 61.7 kJ mol⁻¹, obviously smaller than the values of 89.1 and 122.9 kJ mol⁻¹ for the ultrathin CeO₂ sheets and bulk counterpart. This implied that the CO oxidation catalysed by the ultrathin CeO₂ sheets with numerous surface pits involved different catalytically active sites in comparison with the other two CeO₂ samples⁴⁵, in which the 4-coordinated and 5-coordinated pit-surrounding Ce sites undoubtedly accounted for the eminently lowered apparent activation energy and subsequently decreased CO conversion temperatures. Accordingly, the obviously promoted CO catalytic performances for ultrathin CeO₂ sheets with numerous surface pits were fairly consistent with the corresponding theoretical model predictions, providing strong evidence for the validity and reliability of the designed model. Of note, as shown in Supplementary Fig. S12, one can conclude that the ultrathin CeO₂ sheets with surface-confined pits possessed two types of active sites including very active pit-surrounding Ce atoms and less active surface Ce atoms: when the surface pits had a low percentage such as 2% (Supplementary Fig. S7), the small amount of pit-surrounding Ce atoms and other surface Ce atoms could together act as the active sites to catalyse the CO oxidation reactions; whereas, when the pits occupancy in the ultrathin CeO₂ sheets was up to 10%, the pit-surrounding Ce atoms could serve as the preferentially active sites to support them quickly to complete the CO oxidation reaction in a narrow temperature range (Supplementary Fig. S9).

Discussion

As is well-known, the auto-ignition temperature of CO molecules is as high as 608.89 °C. After adding a catalyst such as bulk CeO₂, the ignition temperature corresponding to 10% CO conversion could be reduced to 281 °C (Fig. 4d), verifying that the catalyst could indeed increase the reaction rate for CO oxidation. More interestingly, our designed three-atom-thick CeO₂ sheets with surface-confined pits further lowered the ignition temperature down to 106 °C. This raises important questions: what causes the strikingly different catalytic activity in the same catalyst material? How does it function? It is noticeable that the catalysis usually occurs at the active sites and the different active sites often lead to distinct CO catalytic reactivities^{15,30,46,47}. Here, DFT calculations in Fig. 4a,b revealed that the pit-surrounding Ce sites confined in atomically thin sheets were identified as the most favourable active centres for CO catalytic oxidation. In addition, the XAFS results in Table 1 showed that the active centres possessed the

average coordination numbers of 4.6, which was much lower than that of other various active sites. Thus, it was the peculiar active centres with lower coordination numbers that brought about the enhanced CO oxidation. In the active centres, the 4- and 5-coordinated pit-surrounding Ce sites favoured for CO adsorption and O₂ activation, respectively, which effectively decreased the catalyst poisoning chance. Also, the highly coordination-unsaturated pit-surrounding Ce sites resulted in the increased carrier density near the Fermi level (Fig. 3c), which ensured fast CO diffusion along the two-dimensional conducting channel of surface pits and subsequently facilitated CO oxidation by the dissociated O atoms^{6,7,32,48}. In other words, the active centres consisting of pit-surrounding Ce sites were beneficial to O₂ activation, CO adsorption and diffusion. In addition, the extremely high fraction of surface Ce atoms as well as the quantum size effect in the ultrathin CeO₂ sheets could also contribute to lower their overall activation energy and definitely accelerate the speed of CO catalytic reaction compared with the bulk counterpart^{24–32}, which could be verified by the CO conversion curves and the corresponding activation energies of the intact ultrathin CeO₂ sheets and bulk counterpart in Fig. 4d,e. As such, the different activation energies between the ultrathin CeO₂ sheets with numerous surface pits and the bulk counterpart were not only due to the presence of surface pits but also due to the quantum effects at the nano-size. That is to say, in the ultrathin CeO₂ sheets with numerous surface pits, the quantum size effect and the abundant highly active pit-surrounding Ce sites could contribute to lower their overall activation energy and definitely increase the speed of CO catalytic reaction. Actually, the experimental results in Fig. 4d,e showed that the apparent activation energy for the ultrathin CeO₂ sheets with numerous surface pits remarkably decreased from 122.9 to 61.7 kJ mol⁻¹, and the corresponding CO conversion temperatures also reduced dramatically as compared to the bulk counterpart, verifying the predictions of the theoretical model. As a consequence, we bridged the gap between theoretical model and real catalyst, and subsequently identified the catalytically active centre through semi-quantifying the model-structure-performance relationship, which deepened our understanding about the underlying nature of catalysis.

In conclusion, conceptually new atomically thin sheets with surface-confined pits were proposed as an excellent platform to study the role of active sites in catalysis. Freestanding three-atom-thick CeO₂ sheets with ~20% surface pits occupancy were synthesized *via* an ‘ultrafast open space transformation’ strategy and taken as an example to semi-quantify the model-structure-performance relationship. XAFS results directly evidenced the lower average coordination number of 4.6 for the abundant pit-surrounding Ce sites, which in fact served as the catalytically active centres. DFT calculations demonstrated that the 4- and 5-coordinated pit-surrounding Ce sites performed their respective functions in CO adsorption and O₂ activation, thus reducing the activation barrier and decreasing the catalyst poisoning chance. Also, the highly coordination-unsaturated pit-surrounding Ce sites brought about the increased hole carrier density and hence assured fast CO diffusion along the two-dimensional conducting channel of surface pits. As a result, the atomically thin CeO₂ sheets with surface-confined pits lowered the apparent activation energy from 122.9 to 61.7 kJ mol⁻¹ and definitely decreased the CO conversion temperatures. This work provides crucial insights into the role of active centres in catalysis through first semi-quantifying the model-structure-performance relationship, opening the door for designing catalytic centres.

Methods

Synthesis details. Synthesis of freestanding ultrathin CeCO₃OH sheets: 1.5 mmol sodium oleate was initially dissolved in 20 ml distilled water. Then, 1 mmol

$\text{CeCl}_3 \cdot 6\text{H}_2\text{O}$ was dissolved in 10 ml distilled water and injected to the above solution followed by vigorous stirring for 30 min. After adding 9 ml $\text{NH}_3 \cdot \text{H}_2\text{O}$ dropwise to the above solution and stirring for 1 h, the mixture was transferred into a 50 ml Teflon-lined autoclave, sealed and heated at 180 °C for 48 h. The system was then allowed to cool down to room temperature naturally, the final product was collected by centrifuging the mixture, washed with cyclohexane for many times and then dried in vacuum overnight for further characterization.

Synthesis of freestanding ultrathin CeO_2 sheets with numerous surface pits: the as-obtained white ultrathin CeCO_3OH sheets were directly heated at 400 °C for 2 min in air and then cooled to room temperature. The brilliant yellow powders were collected for further characterization.

Synthesis of freestanding intact ultrathin CeO_2 sheets: the as-obtained white ultrathin CeCO_3OH sheets were directly heated at 550 °C for 10 s in air and then cooled to room temperature. The brilliant yellow powders were collected for further characterization.

Characterization. XRD patterns were recorded by using a Philips X'Pert Pro Super diffractometer with $\text{Cu K}\alpha$ radiation ($\lambda = 1.54178 \text{ \AA}$). TEM images and high-resolution TEM image were performed by using a JEOL-2010 TEM with an acceleration voltage of 200 kV. The field emission scanning electron microscopy images were performed by using a FEI Sirion-200 SEM. AFM study in the present work was performed by means of Veeco DI Nano-scope MultiMode V system. X-ray photoelectron spectra (XPS) were acquired on an ESCALAB MKII with Mg $\text{K}\alpha$ ($h\nu = 1253.6 \text{ eV}$) as the excitation source. The binding energies obtained in the XPS spectral analysis were corrected for specimen charging by referencing C 1 s to 284.5 eV. The IR spectra were measured on a NICOLET FT-IR spectrometer, using pressed KBr tablets. Raman spectra were detected by a RenishawRM3000 Micro-Raman system. Thermal gravimetric analysis of the as-synthesized samples was carried out on a Shimadzu TA-50 thermal analyser at a heating rate of 10 °C min^{-1} from room temperature to 800 °C. The Ce L_3 -edge XAFS was measured at the 1W1B beamline of Beijing Synchrotron Radiation Factory (BSRF) and the U7C beamline of the National Synchrotron Radiation Laboratory, China. The storage ring of the BSRF was operated at 2.5 GeV with a maximum current of 250 mA, and National Synchrotron Radiation Laboratory was operated with a storage ring working at the energy of 800 MeV and a maximum electron current of 300 mA.

EXAFS data fitting. Note that the HRTEM result in Fig. 2b clearly reveals that the pits possess an occupancy of about 20% in the ultrathin CeO_2 sheets with numerous surface pits. As such, 20% Ce-O distances and coordination numbers surrounding the pits of the ultrathin CeO_2 sheets are regarded to be shrunk during their EXAFS curve-fitting, while the other 80% Ce-O distances and coordination numbers still remain the same as that of intact ultrathin CeO_2 sheets without surface pits.

As shown in Fig. 3b, the FT curve of bulk CeO_2 exhibited two main peaks at 1.95 and 3.65 Å, corresponding to the nearest Ce-O and next nearest Ce-Ce coordinations, respectively. For the ultrathin CeO_2 sheets, the Ce-O and Ce-Ce peak position exhibited a noticeable shift to 1.91 and 3.63 Å, associated with obvious reduction in their peak intensities. Contrastingly, for the ultrathin CeO_2 sheets with numerous surface pits, the intensities of these two peaks further decreased significantly, and most importantly, the Ce-O and Ce-Ce peaks were further shifted to 1.88 and 3.60 Å, qualitatively revealing their different local atomic arrangement compared with ultrathin CeO_2 sheets and bulk counterpart. Moreover, to achieve quantitative structural parameters around Ce atoms in the ultrathin CeO_2 sheets with numerous surface pits, a least-squares curve parameter fitting for the Ce-O, Ce-Ce, Ce-O-O and Ce-Ce-O peaks was conducted. The fitting results for the ultrathin CeO_2 sheets in Table 1 revealed that the distances and coordination numbers for the Ce-O, Ce-Ce, Ce-O-O and Ce-Ce-O coordinations reduced remarkably, while their disorder degrees increased significantly compared with bulk counterpart, suggesting a noticeable distortion on their surface. By contrast, the ultrathin CeO_2 sheets with numerous surface pits possessed further contracted distances and decreased coordination numbers for the Ce-O, Ce-Ce, Ce-O-O and Ce-Ce-O coordinations, along with further increased disorder degrees. Especially, the Ce-O distances surrounding the pits of the ultrathin CeO_2 sheets were obviously contracted from 2.327 to 2.302 Å, and their coordination numbers remarkably decreased from 6.5 to 4.6, associated with significantly increased disorder degrees compared to the ultrathin CeO_2 sheets.

Calculation details. Our first-principles density functional theory (DFT) calculations were performed using a plane wave basis set with the projector augmented plane-wave method^{46–49}. The exchange-correlation interaction is described within the generalized gradient approximation^{50,51}. The energy cutoff is set to 400 eV, and the atomic positions are allowed to relax until the energy and force are less than 10^{-4} eV and $5 \times 10^{-3} \text{ eV \AA}^{-1}$, respectively. The ultrathin CeO_2 sheets with numerous surface pits were simulated by periodically repeating the CeO layers along the [110] direction of the unit cell. Each sheet model consists of three CeO planes and is separated by a vacuum region of 15 Å. An elliptical void area by removing partial surface Ce and O atoms on the ultrathin sheet was used to simulate the pit. For the ultrathin CeO_2 sheets, they were simulated by periodically repeating the CeO layers along the [110] direction of the unit cell. Each sheet

model consists of three CeO planes and is separated by a vacuum region of 15 Å. The comparison calculations for bulk CeO_2 were performed within supercells constructed from a standard unit cell of CeO_2 lattice.

Moreover, we calculated the adsorption energy of CO and O_2 molecules surrounding the pits for various-sized pit models. The adsorption energy ΔE_{ads} is defined as follows:

$$\Delta E_{\text{ads}} = E_{\text{tot}}(\text{NS} + \text{AD}) - E_{\text{tot}}(\text{NS}) - E_{\text{tot}}(\text{AD}) \quad (1)$$

where $E_{\text{tot}}(\text{NS} + \text{AD})$, $E_{\text{tot}}(\text{NS})$ and $E_{\text{tot}}(\text{AD})$ are the total energies of CO and/or O_2 molecule adsorbing on the ultrathin CeO_2 sheet with numerous surface pits, the ultrathin CeO_2 sheet with numerous surface pits, and the adsorbent CO/ O_2 molecules, respectively. The negative value of ΔE_{ads} implies that adsorption is exothermic, so more the negative value of the ΔE_{ads} , more is the stability of the model. Furthermore, the activation barriers of O_2 dissociation were calculated by the climbing image nudged elastic band method^{52,53}, in which the zero energy reference is O_2 in gas phase.

Catalytic activity measurements. The catalytic properties of CO oxidation for CeO_2 were conducted in a quartz-tube plug flow reactor using 50 mg catalyst in a mixed gas of 1 vol% CO and 99 vol% dried air at a flow rate of 40 ml min^{-1} corresponding to a gas hourly space velocity of 48,000 $\text{ml h}^{-1} \text{g}^{-1}$. The catalyst was heated to the desired temperatures at a rate of 2 °C min^{-1} and then kept for 30 min until the catalytic reaction reached a steady state. Then, the composition of effluent gas was analysed by a portable intelligent professional CO_2 detector (Keernuo Gt901, Shenzhen Keernuo Technology Co. Ltd). The CO conversion was calculated from the change in CO_2 concentration of the inlet and outlet gases. Each experiment for the CO conversion was repeated at least three times to ensure reproducibility and to assess the range of experimental errors associated with the experiments, and the experimental error was assessed to be within $\pm 3.0\%$.

References

- Appl, M. 'Ammonia'. in *Ullmann's Encyclopedia of Industrial Chemistry* (Wiley-VCH, Weinheim, Germany, 2006).
- Joo, S. H. *et al.* Size effect of ruthenium nanoparticles in catalytic carbon monoxide oxidation. *Nano Lett.* **10**, 2709–2713 (2010).
- Neitzel, J. J. Enzyme catalysis: the serine proteases. *Nat. Edu.* **3**, 21 (2010).
- Taylor, H. S. A theory of the catalytic surface. *Proc. R. Soc. London, Ser. A* **108**, 105–111 (1925).
- Fu, Q. *et al.* Interface-confined ferrous centres for catalytic oxidation. *Science* **328**, 1141–1144 (2010).
- Sun, Y. F. *et al.* Freestanding tin disulfide single-layers realizing efficient visible-light water splitting. *Angew. Chem. Int. Ed.* **51**, 8727–8731 (2012).
- Sun, Y. F. *et al.* Fabrication of flexible and freestanding zinc chalcogenide single-layers. *Nat. Commun.* **3**, 1057 (2012).
- Dumesic, J. A., Huber, G. W. & Boundart, M. *Principles of Heterogeneous Catalysis* (Wiley-VCH, Weinheim, Germany, 2008).
- Christopher, P., Xin, H. L. & Linic, S. Visible-light-enhanced catalytic oxidation reactions on plasmonic silver nanostructures. *Nat. Chem.* **3**, 467–472 (2011).
- Deng, X. Y., Min, B. K., Guloy, A. & Friend, C. M. Enhancement of O_2 dissociation on Au(111) by adsorbed oxygen: implications for oxidation catalysis. *J. Am. Chem. Soc.* **127**, 9267–9270 (2005).
- Langmuir, I. The mechanism of the catalytic action of platinum in the reactions $2\text{CO} + \text{O}_2 = 2\text{CO}_2$ and $2\text{H}_2 + \text{O}_2 = 2\text{H}_2\text{O}$. *Trans. Farad. Soc.* **17**, 621–654 (1922).
- Hinshelwood, C. N. *The Kinetics of Chemical Change* (Clarendon press, Oxford, UK, 1940).
- Eley, D. D. & Rideal, E. K. Parahydrogen conversion on tungsten. *Nature* **146**, 401–402 (1946).
- Mars, P. & van Krevelen, D. W. Oxidations carried out by means of vanadium oxide catalysts. *Spec. Suppl. Chem. Eng. Sci.* **3**, 41–59 (1954).
- Xie, X. W., Li, Y., Liu, Z. Q., Haruta, M. & Shen, W. J. Low-temperature oxidation of CO catalysed by Co_3O_4 nanorods. *Nature* **458**, 746–749 (2009).
- Leng, M. *et al.* Polyhedral 50-facet Cu_2O microcrystals partially enclosed by {311} high-index planes: synthesis and enhanced catalytic CO oxidation activity. *J. Am. Chem. Soc.* **132**, 17084–17087 (2010).
- Nolan, M. & Watson, G. W. The surface dependence of CO adsorption on Ceria. *J. Phys. Chem. B* **110**, 16600–16606 (2006).
- Huang, M. & Fabris, S. CO adsorption and oxidation on ceria surfaces from DFT + U calculations. *J. Phys. Chem. C* **112**, 8643–8648 (2008).
- Wu, Z. L., Li, M. J. & Overbury, S. H. On the structure dependence of CO oxidation over CeO_2 nanocrystals with well-defined surface planes. *J. Catal.* **285**, 61–73 (2012).
- Wang, X., Jiang, Z. Y., Zheng, B. J., Xie, Z. X. & Zheng, L. S. Synthesis and shape-dependent catalytic properties of CeO_2 nanocubes and truncated octahedral. *CrystEngComm* **14**, 7579–7582 (2012).
- Zhou, K. B., Wang, X., Sun, X. M., Peng, Q. & Li, Y. D. Enhanced catalytic activity of ceria nanorods from well-defined reactive crystal planes. *J. Catal.* **229**, 206–212 (2005).

22. Han, X. G., Li, L. & Wang, C. Synthesis of monodisperse CeO₂ octahedra assembled by nano-sheets with exposed {001} facets and catalytic property. *CrystEngComm* **14**, 1939–1941 (2012).
23. Pan, C. S., Zhang, D. S. & Shi, L. Y. CTAB assisted hydrothermal synthesis, controlled conversion and CO oxidation properties of CeO₂ nanoplates, nanotubes, and nanorods. *J. Solid State Chem.* **181**, 1298–1306 (2008).
24. Carrettin, S., Concepción, P., Corma, A., López Nieto, J. M. & Puentes, V. F. Nanocrystalline CeO₂ increases the activity of Au for CO oxidation by two orders of magnitude. *Angew. Chem. Int. Ed.* **43**, 2538–2540 (2004).
25. González-Rovira, L. *et al.* Single-step process to prepare CeO₂ nanotubes with improved catalytic activity. *Nano. Lett.* **9**, 1395–1400 (2009).
26. Chen, G. *et al.* Interface reaction route to two different kinds of CeO₂ nanotubes. *Inorg. Chem.* **47**, 723–728 (2008).
27. Guo, M. N. *et al.* Nano-sized CeO₂ with extra-high surface area and its activity for CO oxidation. *Mater. Lett.* **64**, 1638–1640 (2010).
28. Lu, X. W., Li, X. Z., Qian, J. C. & Chen, Z. G. The surfactant-assisted synthesis of CeO₂ nanowires and their catalytic performance for CO oxidation. *Powder Technol.* **239**, 415–421 (2013).
29. Huang, X. S. *et al.* Morphology effects of nanoscale ceria on the activity of Au/CeO₂ catalysts for low-temperature CO oxidation. *Appl. Catal. B: Environ.* **90**, 224–232 (2009).
30. Xu, J. H. *et al.* Size dependent oxygen buffering capacity of ceria nanocrystals. *Chem. Commun.* **46**, 1887–1889 (2010).
31. Yeung, C. M. Y. *et al.* Engineering Pt in ceria for a maximum metal support interaction in catalysis. *J. Am. Chem. Soc.* **127**, 18010–18011 (2005).
32. Tsang, S. C., Bulpitt, C. D. A., Mitchell, P. C. H. & Ramirez-Cuesta, A. R. Some new insights into the sensing mechanism of palladium promoted tin (IV) oxide sensor. *J. Phys. Chem. B* **105**, 5737–5742 (2001).
33. Yeung, C. M. Y. & Tsang, S. C. Noble metal core ceria shell catalysts for water gas shift reaction. *J. Phys. Chem. C* **113**, 6074–6087 (2009).
34. McLaren, A., Valdes-Solis, T., Li, G. Q. & Tsang, S. C. Shape and size effects of ZnO nanocrystals on photocatalytic activity. *J. Am. Chem. Soc.* **131**, 12540–12541 (2009).
35. Sun, Y. F., Xie, Y., Wu, C. Z., Zhang, S. D. & Jiang, S. S. Aqueous synthesis of mesostructured BiVO₄ quantum tubes with excellent dual response to visible light and temperature. *Nano Res.* **9**, 620–631 (2010).
36. Sun, Y. F. *et al.* Atomically thick bismuth selenide freestanding single layers achieving enhanced thermoelectric energy harvesting. *J. Am. Chem. Soc.* **134**, 20294–20297 (2012).
37. Park, J. S., Ryu, B., Moon, C. Y. & Chang, K. J. Hole gas induced by defects in Ge/Si core-shell nanowires. *AIP Conf. Proc.* **1399**, 303–304 (2011).
38. Madl, M. *et al.* High resolution photocurrent imaging by atomic force microscopy on the example of single buried InAs quantum dots. *Semicond. Sci. Technol.* **25**, 065010 (2010).
39. Green, I. X., Tang, W. J., Neurock, M. & Yates, Jr J. T. Spectroscopic observation of dual catalytic sites during oxidation of CO on a Au/TiO₂ catalyst. *Science* **333**, 736–739 (2011).
40. Qiao, B. T. *et al.* Single-atom catalysis of CO oxidation using Pt₁/FeO_x. *Nature Chem.* **3**, 634–641 (2011).
41. Wang, L., Zhang, L. F., Zhong, S. L. & Xu, A. W. Highly uniform CeO₂ hierarchical microstructures: Facile synthesis and catalytic activity evaluation. *Appl. Surf. Sci.* **263**, 769–776 (2012).
42. Bao, H. Z. *et al.* Crystal-plane-controlled surface restructuring and catalytic performance of oxide nanocrystals. *Angew. Chem. Int. Ed.* **50**, 12294–12298 (2011).
43. Yoon, B. *et al.* Charging effects on bonding and catalysed oxidation of CO on Au₈ clusters on MgO. *Science* **307**, 403–407 (2005).
44. Minato, T. *et al.* Investigation of the electronic interaction between TiO₂ (110) surfaces and Au clusters by PES and STM. *Surf. Sci.* **566**, 1012–1017 (2004).
45. Babu, S. *et al.* Dopant-mediated oxygen vacancy tuning in ceria nanoparticles. *Nanotechnology* **20**, 085713 (2009).
46. Blochl, P. E. Projector augmented-wave method. *Phys. Rev. B* **50**, 17953–17979 (1994).
47. Kresse, G. & Furthmüller, J. Efficient iterative schemes for ab initio total-energy calculations using a plane-wave basis set. *Phys. Rev. B* **54**, 11169–11186 (1996).
48. Kresse, G. & Furthmüller, J. Efficiency of ab-initio total energy calculations for metals and semiconductors using a plane-wave basis set. *Comput. Mater. Sci.* **6**, 15–50 (1996).
49. Kohn, W. & Sham, L. J. Self-consistent equations including exchange and correlation effects. *Phys. Rev.* **140**, A1133–A1138 (1965).
50. Perdew, J. P. & Wang, Y. Accurate and simple analytic representation of the electron-gas correlation energy. *Phys. Rev. B* **45**, 13244–13249 (1992).
51. Wang, Y. & Perdew, J. P. Correlation hole of the spin-polarized electron gas, with exact small-wave-vector and high-density scaling. *Phys. Rev. B* **44**, 013298–013307 (1991).
52. Henkelman, G., Uberuaga, B. P. & Jónsson, H. A climbing image nudged elastic band method for finding saddle points and minimum energy paths. *J. Chem. Phys.* **113**, 9901–9904 (2000).
53. Ritter, M., Ranke, W. & Weiss, W. Observation of strain-relaxation-induced size effects in p-type Si/SiGe resonant-tunneling diodes. *Phys. Rev. B* **57**, 7140–7140 (1998).

Acknowledgements

We thank Prof. Rui Si in Shanghai Synchrotron Radiation Facility, Chinese Academy of Sciences for his valuable discussion on CO catalytic oxidation. This work was financially supported by National Nature Science Foundation (21331005, 11079004, 21201157, 11135008, 11321503) and Chinese Academy of Science (XDB01020300).

Author contributions

Y.X., S.W. and Y.F.S. conceived the idea and co-wrote the paper. Y.F.S., S.G. and F.C.L. carried out the sample synthesis, characterization and CO catalytic measurement. Z.H.S., H.C. and Y.J. analysed the XAFS data. Q.H.L. and H.B.S. performed the first-principles calculations. All the authors discussed the results, commented on and revised the manuscript.

Additional information

Supplementary Information accompanies this paper at <http://www.nature.com/naturecommunications>

Competing financial interests: The authors declare no competing financial interests.

Reprints and permissions information is available online at <http://npg.nature.com/reprintsandpermissions/>

How to cite this article: Sun, Y. *et al.* Pits confined in ultrathin cerium(IV) oxide for studying catalytic centres in carbon monoxide oxidation. *Nat. Commun.* **4**:2899 doi: 10.1038/ncomms3899 (2013).